

Supercurrent, Multiple Andreev Reflections and Shapiro Steps in InAs Nanosheet Josephson Junctions

Shili Yan,^{†,‡} Haitian Su,^{¶,§,‡} Dong Pan,^{||,‡} Weijie Li,^{¶,⊥} Zhaozheng Lyu,[#] Mo
Chen,[†] Xingjun Wu,[†] Li Lu,[#] Jianhua Zhao,^{*,||} Ji-Yin Wang,^{*,†} and H. Q. Xu^{*,¶,†}

[†]*Beijing Academy of Quantum Information Sciences, 100193 Beijing, China*

[‡]*These authors contribute equally*

[¶]*Beijing Key Laboratory of Quantum Devices, Key Laboratory for the Physics and
Chemistry of Nanodevices, and School of Electronics, Peking University, Beijing 100871,
China*

[§]*Institute of Condensed Matter and Material Physics, School of Physics, Peking University,
Beijing 100871, China*

^{||}*State Key Laboratory of Superlattices and Microstructures, Institute of
Semiconductors, Chinese Academy of Sciences, P.O. Box 912, Beijing 100083, China*

[⊥]*Academy for Advanced Interdisciplinary Studies, Peking University, Beijing 100871, China*

[#]*Beijing National Laboratory for Condensed Matter Physics, Institute of Physics, Chinese
Academy of Sciences; School of Physical Sciences, University of Chinese Academy of
Sciences, Beijing 100190, China*

E-mail: jhzhao@red.semi.ac.cn; wangjiyinshu@gmail.com; hqxu@pku.edu.cn

Abstract

High-quality free-standing InAs nanosheets are emerging layered semiconductor materials with potentials in designing planar Josephson junction devices for novel physics studies due to their unique properties including strong spin-orbit couplings, large Landé g -factors and the two dimensional nature. Here, we report an experimental study of proximity induced superconductivity in planar Josephson junction devices made from free-standing InAs nanosheets. The nanosheets are grown by molecular beam epitaxy and the Josephson junction devices are fabricated by directly contacting the nanosheets with superconductor Al electrodes. The fabricated devices are explored by low-temperature carrier transport measurements. The measurements show that the devices exhibit a gate-tunable supercurrent, multiple Andreev reflections, and a good quality superconductor-semiconductor interface. The superconducting characteristics of the Josephson junctions are investigated at different magnetic fields and temperatures, and are analyzed based on the Bardeen-Cooper-Schrieffer (BCS) theory. The measurements of ac Josephson effect are also conducted under microwave radiations with different radiation powers and frequencies, and integer Shapiro steps are observed. Our work demonstrates that InAs nanosheet based hybrid devices are desired systems for investigating forefront physics, such as the two-dimensional topological superconductivity.

Introduction

Hybrid superconducting devices made from low-dimensional semiconductors with strong spin-orbit couplings, such as InAs and InSb, have attracted great research interests. These devices have now been widely explored for the investigation of exotic physics including anomalous Josephson effect,¹⁻⁴ Josephson diode effect,⁵⁻⁸ and topological superconductivity,⁹⁻¹⁷ and for their potential applications in topological quantum computation.¹⁸⁻²⁰ Many excellent progresses have been achieved in devices made from InAs or InSb nanowires.^{2,11,12,21-26} Comparing to nanowire-based hybrid devices, two-dimensional planar Josephson junctions have the advantage of flexibility for scaling up and it has been shown that the topological phase can be tuned by the phase difference across a planar Josephson junction.¹⁴⁻¹⁶ In addition to nanowires and two-dimensional electron gases (2DEGs) formed in heterostructures, free-standing nanosheets have shown up as an emerging alternative material platform.²⁷⁻³⁰ More than having the same superiorities as 2DEGs mentioned above, nanosheets are capable of being transferred freely, facilitating the fabrication of dual-gate devices. Importantly, spin-orbit interaction, a key parameter in forefront areas of physics, can be tuned by a vertical electric field applied through InAs and InSb nanosheets with the dual-gate architecture.^{31,32} One of the prerequisite conditions to study the diverse physics in semiconductor-superconductor hybrid systems is the induced superconductivity in the semiconductors by proximity effect. Recently, proximity induced superconductivity has been realized in InSb nanosheet Josephson junctions.^{7,33-36} Free-standing InAs nanosheets, on the other hand, appear as contestant materials with the similar intriguing properties as InSb nanosheets.^{29,32,37} However, the proximity induced superconductivity in a free-standing InAs nanosheet, which deserves to be demonstrated as an initial step, has not yet been reported.

Here, we report an experimental study of Josephson junctions made from high-quality, free-standing InAs nanosheets. These nanosheets are grown by molecular-beam epitaxy (MBE) and the devices are fabricated by transferring the nanosheets to a Si/SiO₂ substrate and then by directly contacting the nanosheets with superconductor Al electrodes. The fab-

ricated InAs nanosheet Josephson junction devices are studied by low-temperature carrier transport measurements. The measurements show that these Josephson junction devices exhibit a gate tunable supercurrent (up to ~ 50 nA) and a good interface transparency. Multiple Andreev reflections (MARs) with clear subharmonic peaks at $n = \pm 1, \pm 2, \pm 4$ have shown up. The magnetic field and temperature dependencies of the induced superconductivity are studied, from which a superconducting energy gap of $\Delta \sim 150 \mu\text{eV}$, a critical temperature of $T_c \sim 1.05$ K and a critical magnetic field of $B_c \sim 9.6$ mT are extracted. The InAs nanosheet Josephson junction devices are also investigated under microwave radiations and the ac Josephson effects with clear integer Shapiro steps (up to $n = \pm 5$) are observed. These experimental results show that InAs nanosheets are an excellent material platform for investigating novel superconducting physics, including topological superconductivity.

Results and discussion

The exploited free-standing InAs nanosheets grown by MBE are in wurtzite crystal structure with a thickness ranging from 15 to 30 nm (see Ref. 29 for the details of the InAs nanosheet growth). Figure 1a shows a false-colored scanning electron microscope (SEM) image of a device measured in this work, where the scale bar is 200 nm. Figure 1b shows a cross-sectional schematic view of the device. The InAs nanosheets are mechanically transferred onto a highly n-doped Si substrate, covered by a 300-nm-thick SiO_2 layer on top, which serve as a global back gate in the following measurements. Standard electron-beam lithography is used to pattern the contact areas of the devices. In-situ argon ion milling has been conducted to remove the oxide layer on the surface of the InAs nanosheets prior to deposition of 5-nm-thick Ti and 80-nm-thick Al with electron-beam evaporation. The width of the nanosheet at the junction of a device is ~ 300 nm and the gap between the two superconductor electrode is ~ 90 nm. Electrical measurements on the devices have been performed in a $^3\text{He}/^4\text{He}$ dilution refrigerator at a base temperature of ~ 20 mK. Two comparable devices have been

explored in this work. The results shown in the main article all come from the InAs nanosheet Josephson junction device shown in Figure 1a and the data measured for the other device are presented in the Supporting Information.

Figure 1c shows the measured voltage V across the junction of the hybrid device as a function of bias current I_b in a quasi-four-terminal measurement circuit setup (see details of the measurement setup in Figure S2 in the Supporting Information). The red and blue curves present the results of the measurements in the upward and downward bias current sweeping directions, respectively. Both $V - I_b$ curves show a clear zero voltage region due to a dissipationless supercurrent flow. The switching current I_{sw} and the retrapping current I_{rt} , which are indicated by black arrows, are found to be around 30 nA and 26 nA, respectively, in the device. A hysteretic behavior seen from the upward and downward sweeping measurements, which is commonly observed in nanostructure Josephson junctions,^{23,38} can be explained by phase instability in the junction and/or heating effects.^{39–41} Figure 1d displays a $V - I_b$ trace measured in a larger I_b range (upward sweeping direction only). At sufficiently large I_b , where a voltage drop through the junction is larger than $2\Delta/e$ with Δ being the superconducting gap and e the elementary charge, V appears to show a linear dependence on I_b . By a linear extrapolation from the linear range of the $V - I_b$ curve, excess current I_{ex} , which originates from Cooper pair transport,^{42,43} can be obtained. At the same time, the normal state resistance R_n is extracted from the slope of the linear fit. Here, in Figure 1d, it is found that I_{ex} is about 72 nA and R_n is around 1.82 k Ω . Figure 1e shows the differential resistance dV/dI_b of the device as a function of I_b and back gate voltage V_{bg} (extracted from the upward current sweeping measurements). The center dark area represents that the junction is in the superconducting state and the dark fringes caused by MARs are clearly visible at the outside of the center dark area. The device also exhibits a gate-tunable I_{sw} , which ranges from 27 to 50 nA in the varying region of V_{bg} from -10 to 20 V. Figure 1f displays I_{sw} (red data point) and R_n (blue data point) extracted from Figure 1e as a function V_{bg} . The values of the product $I_{sw}R_n$ obtained from the extracted values

of I_{sw} and R_n shown in Figure 1f are in the range of 50 to 80 μV . In a short, disordered Josephson junction, the product of $I_c R_n$, where I_c is the critical supercurrent, was predicted to be related to the superconducting gap Δ as $I_c R_n = \pi\Delta/2e$.^{39,44} The values of product $I_{sw} R_n$ extracted from our InAs nanosheet Josephson junction device are significantly smaller than the value of $I_c R_n \sim 230 \mu V$, which would be obtained by taking $\Delta \sim 150 \mu eV$ (see Figure 3 below). This discrepancy can be explained by a smaller I_{sw} as compared to I_c due to premature switching.^{23,38}

Figure 1g shows the value of the product $I_{ex} R_n$ as a function of V_{bg} , where I_{ex} and R_n are extracted from the measurements shown in Figure 1e (see Figure 1d and the related text for the extractions of I_{ex} and R_n). It is seen that the value of $I_{ex} R_n$ varies from 113 to 172 μV , which are more comparable to the value of $(\pi^2/4 - 1)\Delta/e \sim 220 \mu V$ predicted for a short disordered junction⁴⁵ than the value of $8\Delta/3e \sim 400 \mu V$ predicted for a short ballistic junction.^{46,47} These experimentally extracted values of $I_{ex} R_n$ can be used to evaluate the transparency of our InAs nanosheet Josephson junctions. The transmission T_r of a Josephson junction can be estimated based on the formula of $T_r = 1/(1 + Z^2)$, where Z is the scattering parameter at the interface between the superconductor and the normal conductor and can be determined from the ratio of $eI_{ex} R_n/\Delta$.^{47,48} In our device, this ratio is found to be in the range of ~ 0.65 to ~ 0.5 , leading to the transmission T_r in a range of $\sim 70\%$ to $\sim 80\%$. Similar values of T_r have been obtained in the second device (see Figure S4 in the Supporting Information). The transparencies of our InAs nanosheet Josephson junction devices are comparable with the values obtained in previous works.^{38,49,50}

In Figure 2, we examine the superconducting characteristics of the InAs nanosheet Josephson junctions at different magnetic fields and temperatures. Figure 2a displays the measured voltage drop V across the Josephson junction shown in Figure 1a as a function of applied bias current I_b at magnetic fields $B = 0$ (blue), $B = 4$ mT (orange) and $B = 13$ mT (red), applied perpendicularly to the InAs nanosheet, and at $V_{bg} = 20$ V. By comparing the three measured $V - I_b$ curves, we see that the switching current is decreased with increasing

magnetic field. Figure 2b shows the differential resistance dV/dI_b as a function of I_b (downward sweeping direction only) and B for the device at $V_{bg} = 20$ V. The center dark blue area presents the superconductive region, with the switching current I_{sw} given by the lower edge of the center area. Figure 2c shows the switching current I_{sw} as a function of B . As shown in Figure 2b and Figure 2c, I_{sw} drops monotonically with increasing B , showing no oscillations. The failure of observing interference patterns could be due to a small junction area so that superconductivity is completely destroyed before the side lobes of a Fraunhofer pattern commence. Similar results are observed in the second device (see details in Figure S5 in the Supporting Information). Figure 2d shows the measured voltage drop V across the junction in the device shown in Figure 1a at three different temperatures $T = 0.02$ K (blue), $T = 0.8$ K (orange) and $T = 1.05$ K (red). As expected, I_{sw} is seen to be smaller at higher temperatures. Figure 2e provides the differential resistance dV/dI_b as a function of I_b (upward sweeping direction only) and T over a larger range of I_b and T . The center dark low-resistance area seen around $I_b \sim 0$ represents that the junction is at the superconducting state and the other low resistance stripes seen at finite I_b originate from multiple Andreev reflections (MARs). Figure 2f displays the switching current I_{sw} (red dots) and the excess current I_{ex} (blue dots) extracted from Figure 2e as a function of temperature T (cf. Figure 1d for the extraction of I_{ex}). As expected, it is seen that both I_{sw} and I_{ex} decrease with increasing T at high temperatures of $T > 0.4$ K. However, in the small temperature region of $T < 0.4$ K, both I_{sw} and I_{ex} are seen to raise with increasing T . The origin of such anomalous enhancements of I_{sw} and I_{ex} is not known to us and thus deserves an investigation in the future.

We now turn to investigate the superconductivity in our InAs nanosheet Josephson junctions in a voltage bias measurement configuration. Figure 3a shows the differential conductance dI_{sd}/dV_{sd} measured for the device shown in Figure 1a as a function of bias voltage V_{sd} at $T \sim 20$ mK, $V_{bg} = 0$ V and $B = 0$ T. The data displays clear peaks with peak positions appearing approximately at $eV_{sd}(n) = 2\Delta/n$, where $n = \pm 1, \pm 2$ and ± 4 , indicated by the

grey dashed lines in the figure. These peaks result from the MAR processes. The clear observation of MARs up to $n = \pm 4$ indicates a high quality and a high interface transparency in the InAs nanosheet Josephson junction. Figure 3b shows a linear fit of peak position (V_{peak}) versus the inversion of the MAR order ($1/n$). The superconducting energy gap extracted from these observed MAR peaks is $\Delta \sim 150 \mu\text{eV}$. Figure 3c shows the differential conductance $dI_{\text{sd}}/dV_{\text{sd}}$ measured for the InAs nanosheet Josephson junction as a function of the bias voltage V_{sd} and temperature T . As T increases, the peak positions move consecutively to lower values of V_{sd} , due to the decrease in the superconducting energy gap Δ with increasing T . According to the prediction of the Bardeen-Cooper-Schrieffer (BCS) theory, the temperature dependence of the superconducting energy gap follows $\Delta(T) = \Delta(0)[\cos[\pi/2(T/T_c)^2]]^{1/2}$, where T_c is the critical temperature of the superconductor.³⁹ The black dashed lines are the fitting results for the positions of the first order peaks, $V_{\text{sd}} = \pm 2\Delta/e$, based on the BCS theoretical prediction. The fitting gives a zero temperature superconducting energy gap of $\Delta(0) \sim 151 \mu\text{eV}$ and a critical temperature of $T_c \sim 1.05 \text{ K}$. Figure 3d shows the differential conductance $dI_{\text{sd}}/dV_{\text{sd}}$ measured for the InAs nanosheet Josephson junction as a function of bias voltage V_{sd} and magnetic field B . Again, the measurements show a few well-resolved MAR peak structures and their magnetic field dependencies follow the evolution of the superconducting energy gap Δ predicted by the BCS theory, $\Delta(B) = \Delta(0)[1 - (B/B_c)^2]^{1/2}$, see the black dashed lines for the theoretical fits to the two first order MAR peaks. The extracted zero field superconducting energy gap $\Delta(0)$ and the critical field B_c from the fits are $\Delta(0) \sim 154 \mu\text{eV}$ and $B_c \sim 9.6 \text{ mT}$.

We have also examined our InAs nanosheet Josephson junction device under microwave radiation and studied the evolution of Shapiro steps at different radiation powers and frequencies. Shapiro step measurements have been used to examine the current-phase relation (CPR), where integer Shapiro steps represent a sinusoidal CPR with a 2π periodicity and half-integer or fractional indexed Shapiro steps indicate a skewed CPR.^{51,52} Furthermore, the missing of odd-integer multiples of Shapiro steps implies a 4π periodical CPR, which

could help to identify the presence of a topological superconducting phase in a Josephson junction.^{53,54,54,55} Figure 4a shows the responses of the InAs nanosheet Josephson junction device shown in Figure 1a in the current bias setup to applied microwave radiations at a frequency of $f = 10$ GHz and powers of (i) $P = -12$ dBm, (ii) $P = -5$ dBm and (iii) $P = 0$ dBm. The red lines are the measured voltage V in units of $hf/2e$ as a function of applied bias current I_b and the blue lines are the extracted differential resistance dV/dI_b . Clear integer voltage steps (integer Shapiro steps) appear at voltage values of $nhf/2e$, where $n = 0, \pm 1$ under the microwave power of -12 dBm, $n = 0, \pm 1, \pm 2, \pm 3$ under the microwave power of -5 dBm, and $n = 0, \pm 1, \pm 2, \pm 3, \pm 4, \pm 5$ under the microwave power of 0 dBm. Figure 4b shows the differential resistance dV/dI_b extracted from the measurements of the device as a function of I_b and microwave power at $f = 10$ GHz. The dark blue, low differential resistance areas marked with integer numbers n are the regions where the integer Shapiro steps are observed. Here, the Shapiro steps up to $n = \pm 5$ can be clearly seen. Such ac Josephson effect measurements have also been carried out at other frequencies for this device and for the second device. Shapiro steps up to high orders can be identified as well in these measurements, see details in Figure S7 in the Supporting Information. The clearly observed integer Shapiro steps reveal the presence of a sinusoidal CPR with a 2π periodicity in our InAs nanosheet Josephson junction devices.

In summary, we have fabricated Al-InAs nanosheet-Al Josephson junction devices and investigated the proximity induced superconductivity in the devices. The switching current I_{sw} is tunable using a back gate and a maximum value of $I_{sw} \sim 50$ nA is observed. The product of the excess current I_{ex} and the normal state resistance R_n as high as ~ 170 μ V is found. We have also observed the well resolved MAR structures of order $n = \pm 1, \pm 2, \pm 4$, verifying a high quality and a high transparency of our Josephson junction devices. The ac Josephson effect is investigated in the devices under microwave radiation and integer Shapiro steps of order n up to ± 5 are observed. The excellent proximity-induced superconducting properties observed in our InAs nanosheet Josephson junction devices show that free-standing

InAs nanosheets can serve as a new material platform for hybrid devices designated for study of novel Josephson junction physics and for realization and manipulation of topological superconducting quantum states.

Author contributions

H.Q.X conceived and supervised the project. S.Y., H.S. and M.C. fabricated the devices with great aids from Z.L and L.L. D.P. and J.Z. grew the semiconductor InAs nanosheets. J.Y.W., W.L. and X.W. set up the microwave radiation measurement circuit in the dilution refrigerator. S.Y., J.Y.W. and H.S. performed the transport measurements. S.Y., J.Y.W. and H.Q.X. analyzed the measurement data. S.Y., J.Y.W. and H.Q.X. wrote the manuscript with inputs from all the authors.

Acknowledgement

This work was supported by the National Natural Science Foundation of China (Grant Nos. 92165208, 11874071, 92065106, 61974138, and 12004039), the Ministry of Science and Technology of China through the National Key Research and Development Program of China (Grant Nos. 2017YFA0303304 and 2016YFA0300601). D.P. also acknowledges the supports from the Youth Innovation Promotion Association, Chinese Academy of Sciences (Nos. 2017156 and Y2021043).

Data analysis and data availability

All details in data analysis are included in a jupyter notebook file. The raw data and the analysis files are available at <https://doi.org/10.5281/zenodo.7837262>.

Conflict of interests

The authors declare no conflict of interests.

References

- (1) Yokoyama, T.; Eto, M.; Nazarov, Y. V. Anomalous Josephson effect induced by spin-orbit interaction and Zeeman effect in semiconductor nanowires. *Phys. Rev. B* **2014**, *89*, 195407.
- (2) Szombati, D.; Nadj-Perge, S.; Car, D.; Plissard, S.; Bakkers, E.; Kouwenhoven, L. Josephson ϕ 0-junction in nanowire quantum dots. *Nat. Phys.* **2016**, *12*, 568–572.
- (3) Strambini, E.; Iorio, A.; Durante, O.; Citro, R.; Sanz-Fernández, C.; Guarcello, C.; Tokatly, I. V.; Braggio, A.; Rocci, M.; Ligato, N., et al. A Josephson phase battery. *Nat. Nanotechnol.* **2020**, *15*, 656–660.
- (4) Mayer, W.; Dartiailh, M. C.; Yuan, J.; Wickramasinghe, K. S.; Rossi, E.; Shabani, J. Gate controlled anomalous phase shift in Al/InAs Josephson junctions. *Nat. Commun.* **2020**, *11*, 212.
- (5) Chen, C.-Z.; He, J. J.; Ali, M. N.; Lee, G.-H.; Fong, K. C.; Law, K. T. Asymmetric Josephson effect in inversion symmetry breaking topological materials. *Phys. Rev. B* **2018**, *98*, 075430.
- (6) Baumgartner, C.; Fuchs, L.; Costa, A.; Reinhardt, S.; Gronin, S.; Gardner, G. C.; Lindemann, T.; Manfra, M. J.; Faria Junior, P. E.; Kochan, D., et al. Supercurrent rectification and magnetochiral effects in symmetric Josephson junctions. *Nat. Nanotechnol.* **2022**, *17*, 39–44.
- (7) Turini, B.; Salimian, S.; Carrega, M.; Iorio, A.; Strambini, E.; Giazotto, F.; Zannier, V.;

- Sorba, L.; Heun, S. Josephson Diode Effect in High-Mobility InSb Nanoflags. *Nano Lett.* **2022**, *22*, 8502–8508.
- (8) Mazur, G.; van Loo, N.; van Driel, D.; Wang, J.-Y.; Badawy, G.; Gazibegovic, S.; Bakkers, E.; Kouwenhoven, L. The gate-tunable Josephson diode. *arXiv:2211.14283* **2022**,
- (9) Lutchyn, R. M.; Sau, J. D.; Sarma, S. D. Majorana fermions and a topological phase transition in semiconductor-superconductor heterostructures. *Phys. Rev. Lett.* **2010**, *105*, 077001.
- (10) Oreg, Y.; Refael, G.; Von Oppen, F. Helical liquids and Majorana bound states in quantum wires. *Phys. Rev. Lett.* **2010**, *105*, 177002.
- (11) Mourik, V.; Zuo, K.; Frolov, S. M.; Plissard, S.; Bakkers, E. P.; Kouwenhoven, L. P. Signatures of Majorana fermions in hybrid superconductor-semiconductor nanowire devices. *Science* **2012**, *336*, 1003–1007.
- (12) Deng, M. T.; Yu, C. L.; Huang, G. Y.; Larsson, M.; Caroff, P.; Xu, H. Q. Anomalous zero-bias conductance peak in a Nb–InSb nanowire–Nb hybrid device. *Nano Lett.* **2012**, *12*, 6414–6419.
- (13) Deng, M. T.; Yu, C. L.; Huang, G. Y.; Larsson, M.; Caroff, P.; Xu, H. Q. Parity independence of the zero-bias conductance peak in a nanowire based topological superconductor-quantum dot hybrid device. *Sci. Rep.* **2014**, *4*, 7261.
- (14) Pientka, F.; Keselman, A.; Berg, E.; Yacoby, A.; Stern, A.; Halperin, B. I. Topological superconductivity in a planar Josephson junction. *Phys. Rev. X* **2017**, *7*, 021032.
- (15) Fornieri, A.; Whiticar, A. M.; Setiawan, F.; Portolés, E.; Drachmann, A. C.; Keselman, A.; Gronin, S.; Thomas, C.; Wang, T.; Kallaher, R., et al. Evidence of topological superconductivity in planar Josephson junctions. *Nature* **2019**, *569*, 89–92.

- (16) Ren, H.; Pientka, F.; Hart, S.; Pierce, A. T.; Kosowsky, M.; Lunczer, L.; Schlereth, R.; Scharf, B.; Hankiewicz, E. M.; Molenkamp, L. W., et al. Topological superconductivity in a phase-controlled Josephson junction. *Nature* **2019**, *569*, 93–98.
- (17) Aghaee, M.; Akkala, A.; Alam, Z.; Ali, R.; Ramirez, A. A.; Andrzejczuk, M.; Antipov, A. E.; Astafev, M.; Bauer, B.; Becker, J., et al. InAs-Al hybrid devices passing the topological gap protocol. *arXiv:2207.02472* **2022**,
- (18) Nayak, C.; Simon, S. H.; Stern, A.; Freedman, M.; Sarma, S. D. Non-Abelian anyons and topological quantum computation. *Rev. Mod. Phys.* **2008**, *80*, 1083.
- (19) Stern, A.; Lindner, N. H. Topological quantum computation—from basic concepts to first experiments. *Science* **2013**, *339*, 1179–1184.
- (20) Schrade, C.; Fu, L. Majorana superconducting qubit. *Phys. Rev. Lett.* **2018**, *121*, 267002.
- (21) Nilsson, H. A.; Caroff, P.; Thelander, C.; Larsson, M.; Wagner, J. B.; Wernersson, L.-E.; Samuelson, L.; Xu, H. Q. Giant, Level-Dependent g Factors in InSb Nanowire Quantum Dots. *Nano Lett.* **2009**, *9*, 3151–3156.
- (22) Nilsson, H. A.; Caroff, P.; Thelander, C.; Larsson, M.; Wagner, J. B.; Wernersson, L.-E.; Samuelson, L.; Xu, H. Q. Correlation-Induced Conductance Suppression at Level Degeneracy in a Quantum Dot. *Phys. Rev. Lett.* **2010**, *104*, 186804.
- (23) Nilsson, H. A.; Samuelsson, P.; Caroff, P.; Xu, H. Q. Supercurrent and multiple Andreev reflections in an InSb nanowire Josephson junction. *Nano Lett.* **2012**, *12*, 228–233.
- (24) Abay, S.; Nilsson, H. A.; Wu, F.; Xu, H. Q.; Wilson, C. M.; Delsing, P. High critical-current superconductor-InAs nanowire-superconductor junctions. *Nano Lett.* **2012**, *12*, 5622–5625.

- (25) Abay, S.; Persson, D.; Nilsson, H.; Xu, H. Q.; Fogelström, M.; Shumeiko, V.; Delsing, P. Quantized conductance and its correlation to the supercurrent in a nanowire connected to superconductors. *Nano Lett.* **2013**, *13*, 3614–3617.
- (26) Albrecht, S. M.; Higginbotham, A. P.; Madsen, M.; Kuemmeth, F.; Jespersen, T. S.; Nygård, J.; Krogstrup, P.; Marcus, C. Exponential protection of zero modes in Majorana islands. *Nature* **2016**, *531*, 206–209.
- (27) Pan, D.; Fan, D.; Kang, N.; Zhi, J.; Yu, X.; Xu, H. Q.; Zhao, J. Free-standing two-dimensional single-crystalline InSb nanosheets. *Nano Lett.* **2016**, *16*, 834–841.
- (28) De La Mata, M.; Leturcq, R.; Plissard, S. R.; Rolland, C.; Magén, C.; Arbiol, J.; Caroff, P. Twin-induced InSb nanosails: A convenient high mobility quantum system. *Nano Lett.* **2016**, *16*, 825–833.
- (29) Pan, D.; Wang, J.-Y.; Zhang, W.; Zhu, L.; Su, X.; Fan, F.; Fu, Y.; Huang, S.; Wei, D.; Zhang, L., et al. Dimension engineering of high-quality InAs nanostructures on a wafer scale. *Nano Lett.* **2019**, *19*, 1632–1642.
- (30) Sun, Q.; Gao, H.; Zhang, X.; Yao, X.; Xu, S.; Zheng, K.; Chen, P.; Lu, W.; Zou, J. High-quality epitaxial wurtzite structured InAs nanosheets grown in MBE. *Nanoscale* **2020**, *12*, 271–276.
- (31) Chen, Y.; Huang, S.; Pan, D.; Xue, J.; Zhang, L.; Zhao, J.; Xu, H. Q. Strong and tunable spin-orbit interaction in a single crystalline InSb nanosheet. *NPJ 2D Mater. Appl.* **2021**, *5*, 3.
- (32) Fan, F.; Chen, Y.; Pan, D.; Zhao, J.; Xu, H. Q. Electrically tunable spin-orbit interaction in an InAs nanosheet. *Nanoscale Advances* **2022**, *4*, 2642–2648.
- (33) Kang, N.; Fan, D.; Zhi, J.; Pan, D.; Li, S.; Wang, C.; Guo, J.; Zhao, J.; Xu, H. Q. Two-

- dimensional quantum transport in free-standing InSb nanosheets. *Nano letters* **2018**, *19*, 561–569.
- (34) Zhi, J.; Kang, N.; Li, S.; Fan, D.; Su, F.; Pan, D.; Zhao, S.; Zhao, J.; Xu, H. Q. Supercurrent and multiple Andreev reflections in InSb nanosheet SNS junctions. *Phys. Status. Solidi (B)* **2019**, *256*, 1800538.
- (35) Salimian, S.; Carrega, M.; Verma, I.; Zannier, V.; Nowak, M. P.; Beltram, F.; Sorba, L.; Heun, S. Gate-controlled supercurrent in ballistic InSb nanoflag Josephson junctions. *Appl. Phys. Lett.* **2021**, *119*, 214004.
- (36) Iorio, A.; Crippa, A.; Turini, B.; Salimian, S.; Carrega, M.; Chiroli, L.; Zannier, V.; Sorba, L.; Strambini, E.; Giazotto, F., et al. Half-integer Shapiro steps in highly transmissive InSb nanoflag Josephson junctions. *arXiv:2303.05951* **2023**,
- (37) Fan, F.; Chen, Y.; Pan, D.; Zhao, J.; Xu, H. Q. Measurements of spin-orbit interaction in epitaxially grown InAs nanosheets. *Appl. Phys. Lett.* **2020**, *117*, 132101.
- (38) Doh, Y.-J.; van Dam, J. A.; Roest, A. L.; Bakkers, E. P.; Kouwenhoven, L. P.; De Franceschi, S. Tunable supercurrent through semiconductor nanowires. *Science* **2005**, *309*, 272–275.
- (39) Tinkham, M. *Introduction to superconductivity*; Courier Corporation, 2004.
- (40) Tinkham, M.; Free, J.; Lau, C.; Markovic, N. Hysteretic I- V curves of superconducting nanowires. *Phys. Rev. B* **2003**, *68*, 134515.
- (41) Courtois, H.; Meschke, M.; Peltonen, J.; Pekola, J. P. Origin of hysteresis in a proximity Josephson junction. *Phys. Rev. Lett.* **2008**, *101*, 067002.
- (42) Bratus, E.; Shumeiko, V.; Wendin, G. Theory of subharmonic gap structure in superconducting mesoscopic tunnel contacts. *Phys. Rev. Lett.* **1995**, *74*, 2110.

- (43) Cuevas, J.; Martín-Rodero, A.; Yeyati, A. L. Hamiltonian approach to the transport properties of superconducting quantum point contacts. *Phys. Rev. B* **1996**, *54*, 7366.
- (44) Beenakker, C. W. J. Universal limit of critical-current fluctuations in mesoscopic Josephson junctions. *Phys. Rev. Lett.* **1991**, *67*, 3836.
- (45) Artemenko, S.; Volkov, A.; Zaitsev, A. Theory of the nonstationary Josephson effect in short superconducting contacts. *Zhurnal Eksperimental'noi i Teoreticheskoi Fiziki* **1979**, *76*, 1816–1833.
- (46) Klapwijk, T.; Blonder, G.; Tinkham, M. Explanation of subharmonic energy gap structure in superconducting contacts. *Physica B+ C* **1982**, *109*, 1657–1664.
- (47) Flensberg, K.; Hansen, J. B.; Octavio, M. Subharmonic energy-gap structure in superconducting weak links. *Phys. Rev. B* **1988**, *38*, 8707.
- (48) Blonder, G.; Tinkham, M.; Klapwijk, T. Transition from metallic to tunneling regimes in superconducting microconstrictions: Excess current, charge imbalance, and supercurrent conversion. *Phys. Rev. B* **1982**, *25*, 4515.
- (49) Li, S.; Kang, N.; Fan, D.; Wang, L.; Huang, Y.; Caroff, P.; Xu, H. Q. Coherent charge transport in ballistic InSb nanowire Josephson junctions. *Sci. Rep.* **2016**, *6*, 24822.
- (50) Nishio, T.; Kozakai, T.; Amaha, S.; Larsson, M.; Nilsson, H. A.; Xu, H. Q.; Zhang, G.; Tateno, K.; Takayanagi, H.; Ishibashi, K. Supercurrent through inas nanowires with highly transparent superconducting contacts. *Nanotechnol.* **2011**, *22*, 445701.
- (51) Dinsmore III, R. C.; Bae, M.-H.; Bezryadin, A. Fractional order Shapiro steps in superconducting nanowires. *Appl. Phys. Lett.* **2008**, *93*, 192505.
- (52) Raes, B.; Tubsrinuan, N.; Sreedhar, R.; Guala, D.; Panghotra, R.; Dausy, H.; de Souza Silva, C. C.; Van de Vondel, J. Fractional Shapiro steps in resistively shunted

Josephson junctions as a fingerprint of a skewed current-phase relationship. *Phys. Rev. B* **2020**, *102*, 054507.

- (53) Rokhinson, L. P.; Liu, X.; Furdyna, J. K. The fractional ac Josephson effect in a semiconductor–superconductor nanowire as a signature of Majorana particles. *Nat. Phys.* **2012**, *8*, 795–799.
- (54) Wiedenmann, J.; Bocquillon, E.; Deacon, R. S.; Hartinger, S.; Herrmann, O.; Klapwijk, T. M.; Maier, L.; Ames, C.; Brüne, C.; Gould, C., et al. 4π -periodic Josephson supercurrent in HgTe-based topological Josephson junctions. *Nat. Commun.* **2016**, *7*, 10303.
- (55) Rosenbach, D.; Schmitt, T. W.; Schüffelgen, P.; Stehno, M. P.; Li, C.; Schleenvoigt, M.; Jalil, A. R.; Mussler, G.; Neumann, E.; Trelenkamp, S., et al. Reappearance of first Shapiro step in narrow topological Josephson junctions. *Sci. Adv.* **2021**, *7*, eabf1854.

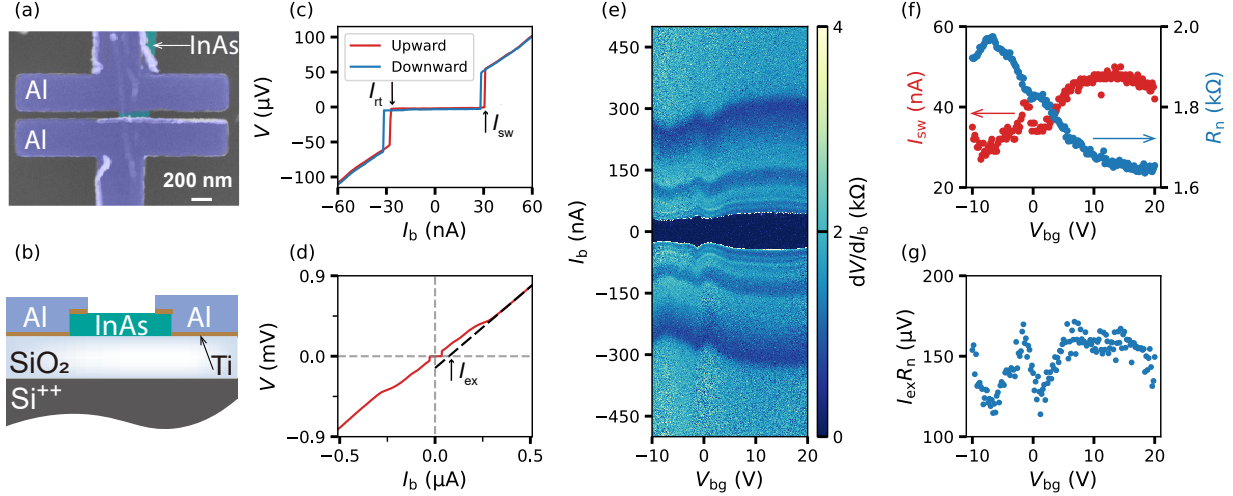


Figure 1: **(a)** False colored SEM image of an InAs nanosheet Josephson junction device with the measurement data presented in the main article. The device is made on a heavily n-doped Si/SiO₂ substrate. The InAs nanosheet is colored in green. The source and drain electrodes are colored in light blue and are made of Ti/Al (5 nm/80 nm in thickness). The scale bar is 200 nm. **(b)** Cross-sectional schematic view of the device. **(c)** Measured voltage V across the junction as a function of bias current I_b at back gate voltage $V_{bg} = 0$. The red and blue lines represent the measurements taken with the upward and downward current sweeping directions, respectively. The switching current I_{sw} and the retrapping current I_{re} are indicated with black arrows. **(d)** V - I_b curve in a larger I_b sweeping range. The black dashed line is a linear fit the V - I_b curve in a range where V is larger than $2\Delta/e$. The fitting line extrapolates to a finite current (i.e., excess current I_{ex}) at $V = 0$, while the slope of the fitting line gives the resistance R_n of the junction in the normal state. **(e)** Differential resistance dV/dI_b , on a color scale, as a function of V_{bg} and I_b (upward current sweeping direction only). The central dark area is the region of $dV/I_b = 0$ where the Josephson junction is in the superconducting state. **(f)** Switching current I_{sw} (red dots) and normal state resistance R_n (blue dots) extracted from the measurements in (e) as a function of V_{bg} . **(g)** $I_{ex}R_n$ product extracted from (e) as a function of V_{bg} . All data here is measured at $B = 0$ and base temperature $T \sim 20$ mK.

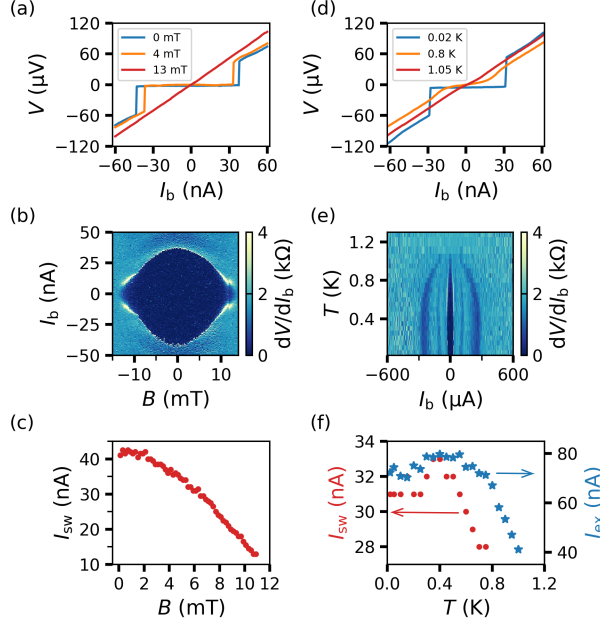


Figure 2: **(a)** Measured voltage V as a function of bias current I_b at different magnetic fields B . Here, at each magnetic field, only the measurements with sweeping current downward are shown. **(b)** Differential resistance dV/dI_b , on a colour scale, as a function of magnetic field B and bias current I_b (only the measurements with sweeping current downward are shown). The central dark blue area is the superconducting region with $dV/dI_b = 0$. The measurements data shown in (a) and (b) are taken at $V_{bg} = 20$ V and base temperature $T \sim 20$ mK. **(c)** Switching current I_{sw} extracted from the measurement in (b) as a function of magnetic field B . **(d)** Measured voltage V as a function of bias current I_b at different temperatures T . Here, at each temperature, only the measurements with sweeping current downward are shown. **(e)** Differential resistance dV/dI_b , on a colour scale, as a function of bias current I_b (data with upward current sweeping direction only) and temperature T . The central dark blue area is the superconducting region with $dV/dI_b = 0$. The measurements data shown in (d) and (e) are taken at $V_{bg} = 0$ and $B = 0$. **(f)** Switching current I_{sw} and excess current I_{ex} as a function of temperature T . I_{sw} is extracted from right the edge of the center dark area in (e) and I_{ex} is extracted from the measurements in (e) with the method illustrated in Figure 1d.

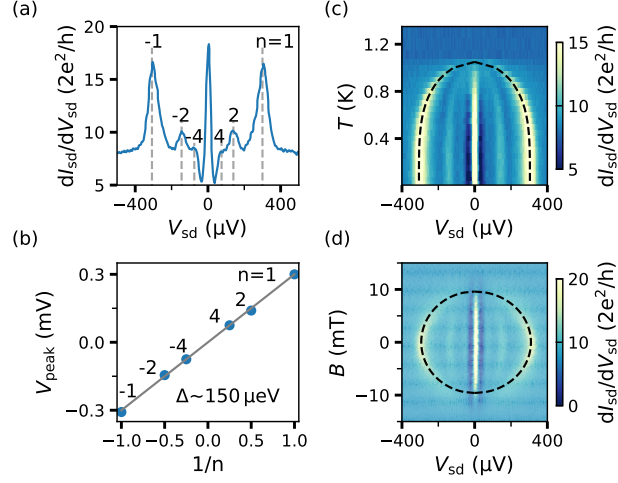


Figure 3: **(a)** Differential conductance dI_{sd}/dV_{sd} as a function of source drain voltage V_{sd} measured at $V_{bg} = 0$, $B = 0$ and base temperature $T \sim 20$ mK. The vertical grey dashed lines mark the peak positions of MAR peaks, and the integer numbers n represent the orders of the MARs. **(b)** Plot of the MAR peak position (V_{peak}) against the inverse MAR order $1/n$. The grey line is the linear fit of data. The superconducting energy gap Δ determined from the slope of the fitting line is $\Delta \sim 150 \mu eV$. **(c)** Differential conductance dI_{sd}/dV_{sd} measured as a function of V_{sd} and T at $V_{bg} = 0$ and $B = 0$. The black dashed line is the fitting curve of the first-order MAR peak positions, $V_{sd} = \pm 2\Delta/e$, to the BCS theory. **(d)** Differential conductance dI_{sd}/dV_{sd} measured as a function of V_{sd} and magnetic field B at $V_{bg} = 0$ and $T \sim 20$ mK. The black dashed line is the fitting curve of the first-order MAR positions, $V_{sd} = \pm 2\Delta/e$, to the BCS theory.

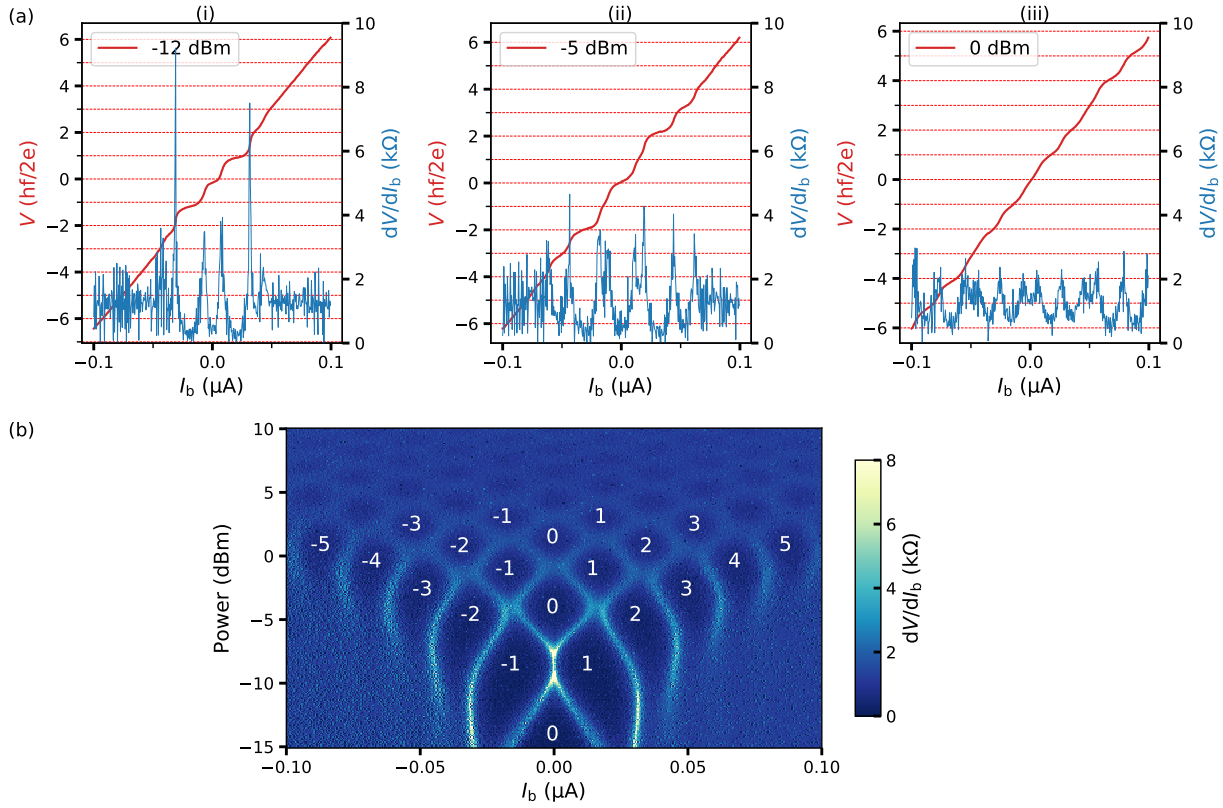


Figure 4: ac Josephson effect measured under microwave radiation of frequency $f = 10$ GHz at $B = 0$ and $T \sim 20$ mK. **(a)** Measured voltage V in units of $hf/2e$ (red lines) and extracted differential resistance dV/dI_b (blue lines) as a function of bias current I_b under microwave powers of (i) -12 dBm, (ii) -5 dBm and (iii) 0 dBm. Here, the integer Shapiro steps of several orders n at voltages $V = nhf/2e$ are clearly visible. **(b)** Differential resistance dV/dI_b , on a color scale, as a function of bias current I_b and microwave power. The dark blue areas marked with integer numbers n are the regions where the integer Shapiro steps are found.

Supporting Information: Supercurrent, Multiple Andreev Reflections and Shapiro Steps in InAs Nanosheet Josephson Junctions

Shili Yan,^{†,‡} Haitian Su,^{¶,§,‡} Dong Pan,^{||,‡} Weijie Li,^{¶,⊥} Zhaozheng Lyu,[#] Mo
Chen,[†] Xingjun Wu,[†] Li Lu,[#] Jianhua Zhao,^{*,||} Ji-Yin Wang,^{*,†} and H. Q. Xu^{*,¶,†}

[†]*Beijing Academy of Quantum Information Sciences, 100193 Beijing, China*

[‡]*These authors contribute equally*

[¶]*Beijing Key Laboratory of Quantum Devices, Key Laboratory for the Physics and
Chemistry of Nanodevices, and School of Electronics, Peking University, Beijing 100871,
China*

[§]*Institute of Condensed Matter and Material Physics, School of Physics, Peking University,
Beijing 100871, China*

^{||}*State Key Laboratory of Superlattices and Microstructures, Institute of
Semiconductors, Chinese Academy of Sciences, P.O. Box 912, Beijing 100083, China*

[⊥]*Academy for Advanced Interdisciplinary Studies, Peking University, Beijing 100871, China*

[#]*Beijing National Laboratory for Condensed Matter Physics, Institute of Physics, Chinese
Academy of Sciences; School of Physical Sciences, University of Chinese Academy of
Sciences, Beijing 100190, China*

E-mail: jhzhao@red.semi.ac.cn; wangjiyinshu@gmail.com; hqxu@pku.edu.cn

Methodes

Material growth

Free-standing InAs nanosheets are grown on a p-type Si(111) substrate by MBE at a temperature of 545 °C, see Ref. 29 in the main article for detailed information. Figure S1(a) shows a scanning electron microscope (SEM) image (side view) of InAs nanosheets on the growth substrate. Figure S1(b) shows a transmission electron microscopy (TEM) image of a typical InAs nanosheet. Figure S1(c) displays a corresponding selected-area electron diffraction (SAED) pattern recorded along the $[2-1-10]$ crystallographic direction of the InAs nanosheet. Figure S1(d) shows a high-resolution TEM image of the nanosheet, which verifies the high quality of the crystal with nearly no stacking faults and twin defects.

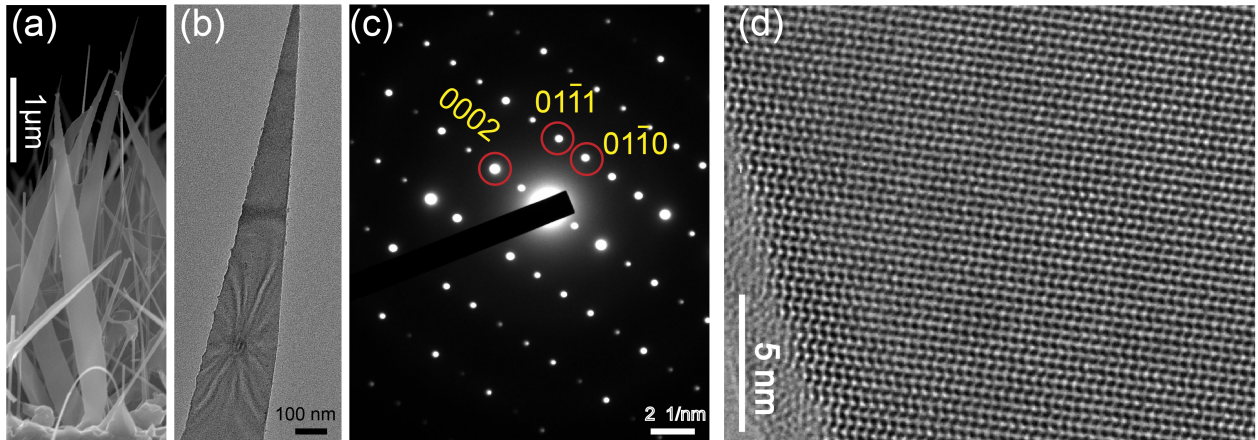


Figure S1: (a) SEM image (side view) of InAs nanosheets on the grown substrate. (b) Overview TEM image of a typical InAs nanosheet. (c) SAED pattern of the InAs nanosheet. (d) High resolution TEM image of the InAs nanosheet.

Device fabrication

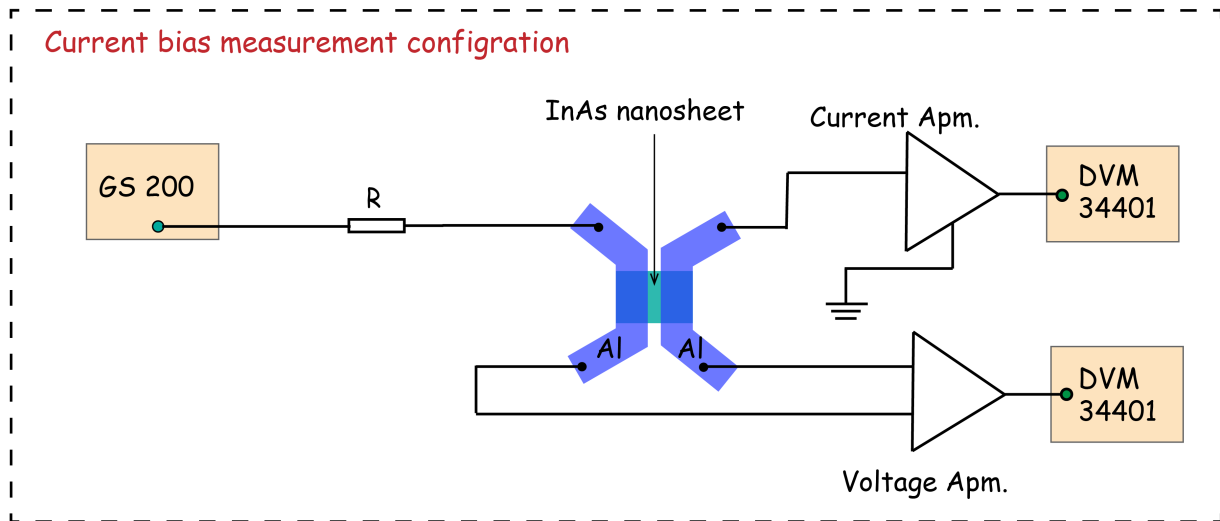
InAs nanosheets are mechanically transferred onto a degenerately n-doped Si substrate, capped with a 300 nm thick layer of SiO₂ on top, with pre-patterned Ti/Au markers on the surface. The highly doped Si and the 300 nm thick SiO₂ are used as a global back gate and the gate dielectric, respectively. SEM is used to select suitable InAs nanosheets for device fabrication. PMMA A4 with a thickness of about 200 nm is spin coated on the surface and

then baked at a temperature of 170°C for 3 minutes. Standard electron-beam lithography is used to pattern the device contact areas on the PMMA. The patterned sample is then developed in a standard development process in developer MIBK : IPA = 1 : 3 at room temperature. In-situ argon ion milling is used to remove the oxide layer on the opened surface of the InAs nanosheets right before deposition of 5 nm/80 nm of Ti/Al by e-beam evaporation. The sample is then bathed in acetone for lift off and cleaned by rinsing in isopropyl alcohol. A room temperature probe station is employed to measure the resistance of the devices fabricated on the chip and devices with a resistance of about 1 ~ 2 k Ω are selected for low temperature transport measurements. A SEM image of a typical device, which is also the device with the measurements reported in the main article, is shown in Figure 1(a) of the main article. Note that the SEM image of the device is taken after all the low temperature transport measurements are made.

Low temperature transport measurements

Devices are measured in a dilution refrigerator equipped with a magnet. Two different measurement configurations are used in this work. The first one is a dc current bias configuration, see Figure S2(a). In this configuration, a quasi-four-terminal measurement setup is employed. The source-drain current is pre-amplified by 10^6 A/V and the measured voltage is pre-amplified by setting a gain at 100 [with an actual gain at ~ 117 , see Figure S3(a) and Figure S3(b)]. The second one is a voltage bias configuration, see Figure S2(b). In this configuration, a two-terminal measurement setup is employed and the measurements are performed using a standard lock-in technique by applying a (dc+ac) bias voltage to the source contact, see Figure S2(b). Here, a serial resistance of 422 Ω from the measurement circuit has been subtracted. Figure S3(c) and Figure S3(d) show the circuit for the measurement of the serial resistance of the measurement circuit and how the serial resistance value is extracted. The value of the magnetic field is calibrated by an offset of -6 mT.

(a)



(b)

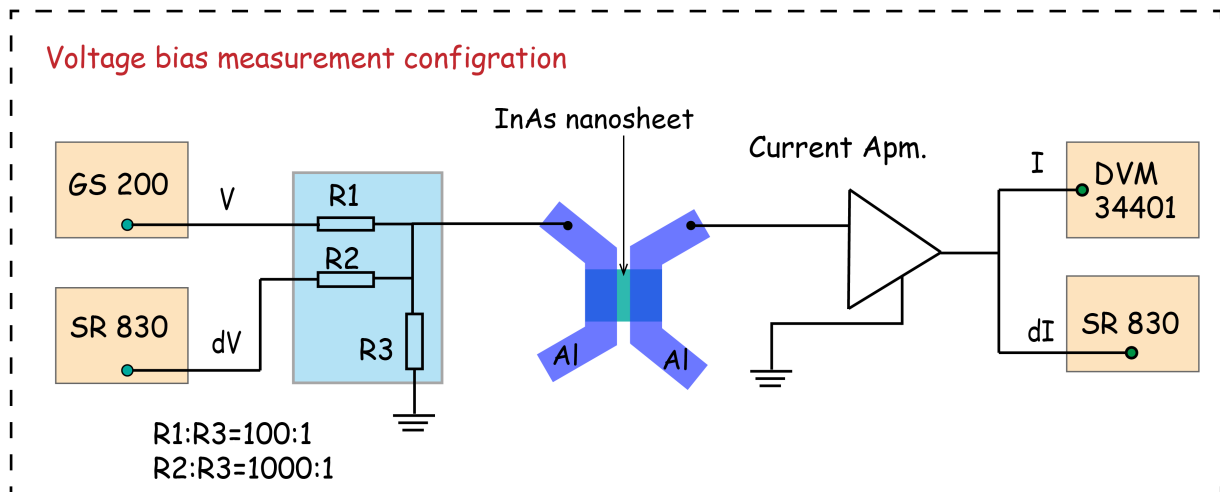


Figure S2: (a) Measurement circuit setup for the current bias configuration. (b) Measurement circuit setup for the voltage bias configuration.

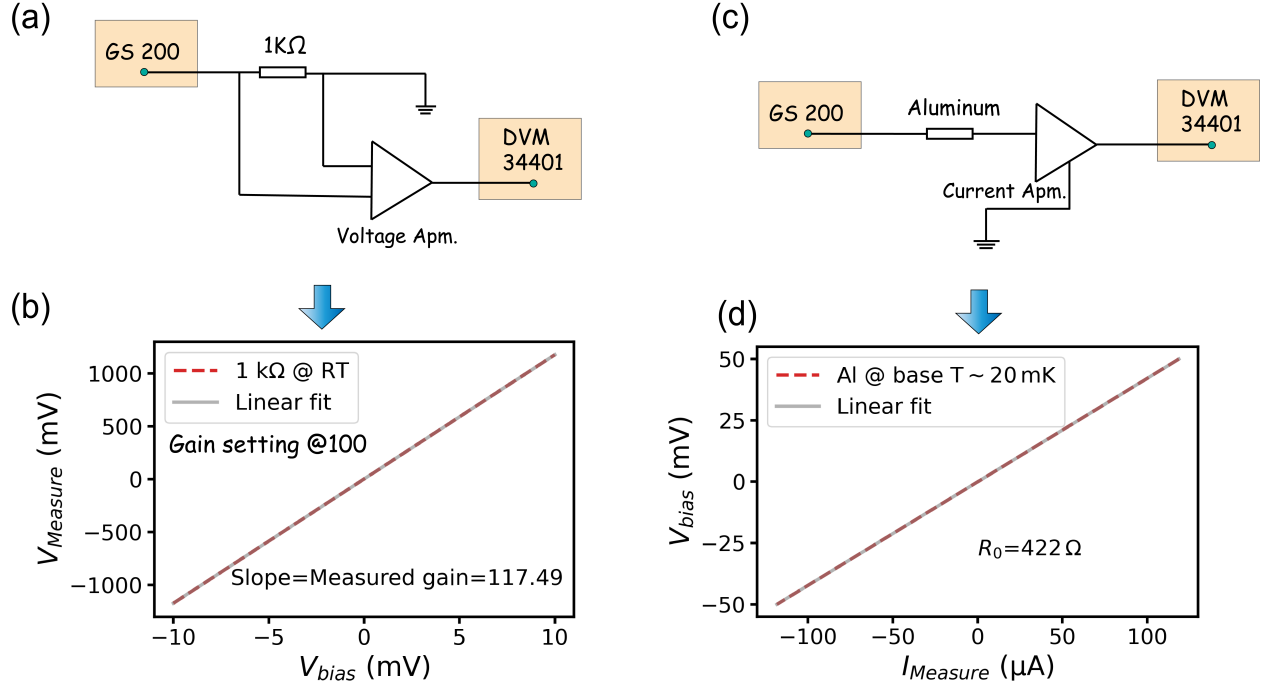


Figure S3: (a) Measurement circuit setup for calibration of the voltage amplifier. (b) Measured voltage V_{Measure} with a voltage pre-amplifier (with a gain set at 100) as a function of bias voltage V_{bias} (red dashed line). The slope of the linear fit represents the actual gain of the voltage pre-amplifier at a setting gain of 100, which is 117. (c) Measurement circuit setup for calibrating the serial resistance in the measurement circuit. (d) Plot of voltage bias V_{bias} versus measured current I_{Measure} of an aluminum strip with a two-terminal configuration at a temperature of $\sim 20\text{ mK}$. The resistance of the aluminum strip is zero for the fact that it is at the superconducting state. Thus, the slope of the linear fit of the measured curve corresponds to the serial resistance in the measurement circuit, which is $422\ \Omega$.

Additional data

The measurement data presented in the main article all come from the InAs nanosheet Josephson junction device shown in Figure 1(a) of the main article (denoted as device D1). Here we display the measurement data from the second device (denoted as device D2) as well as some additional measurement data from device D1. Devices D2 and D1 are fabricated at the same time on the same substrate with the same fabrication process.

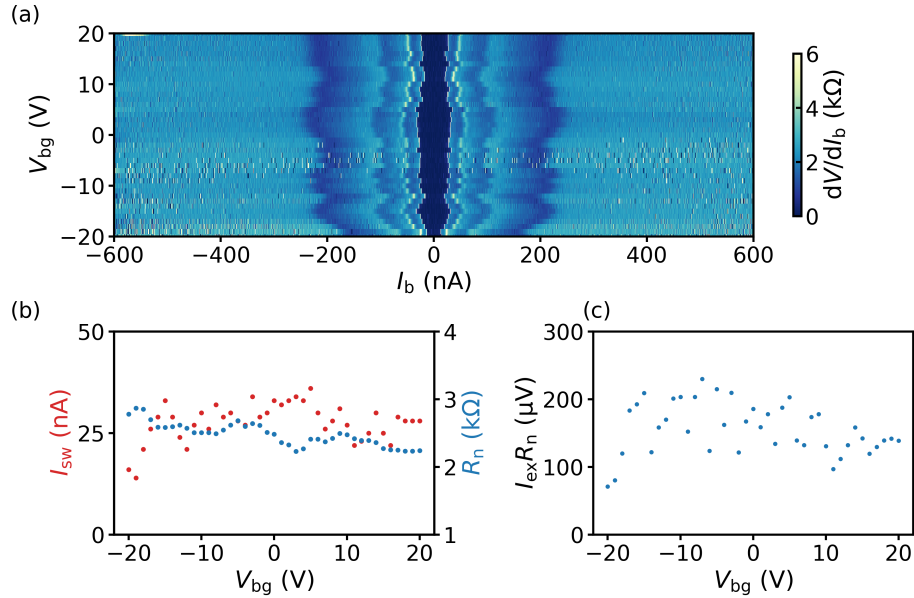


Figure S4: **Gate dependent supercurrent measurements of device D2.** (a) Differential resistance dV/dI_b as a function of bias current I_b and back gate voltage V_{bg} (upward current sweeping direction only). The central dark area is the superconducting region with $dV/I_b = 0$. The switching current I_{sw} can be extracted from the right edge of the centre dark area, which varies with V_{bg} . (b) I_{sw} and normal state resistance R_n extracted from (a) as a function of V_{bg} . The value of the $I_{sw}R_n$ product fluctuates in a range between $40 \mu eV$ and $90 \mu eV$ as V_{bg} varies from $-20 V$ to $20 V$. (c) $I_{ex}R_n$ product as a function of V_{bg} , where I_{ex} is the excess current extracted from (a). The value of $I_{ex}R_n$ varies between $70 \mu eV$ and $230 \mu eV$, leading to that the interface transparency of the device varies in a range between 60% and 86% . All data are measured at $B = 0$ and $T \sim 20 mK$.

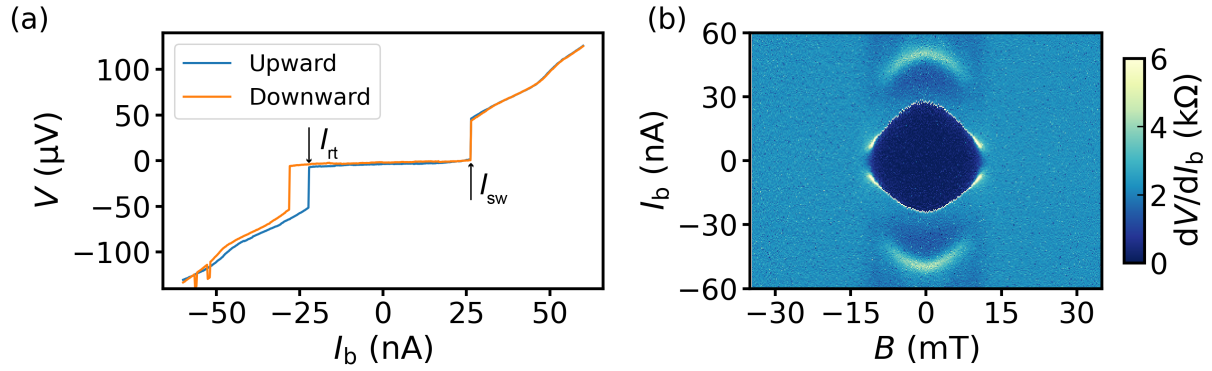


Figure S5: **Hysteresis behavior and magnetic field dependent measurements of device D2 in the current bias configuration.** (a) Voltage V across the junction as a function of bias current I_b measured for both upward and downward current sweep directions. The data show a similar hysteresis behaviour as device D1. (b) Differential resistance dV/dI_b as a function of bias current I_b and magnetic field B . The central dark area corresponds to the region where the junction is at the superconducting state with $dV/dI_b = 0$. The upper and lower fringes are due to multiple Andreev reflections. Here, the Same as device D1, no side lobes of the Fraunhofer pattern is observed.

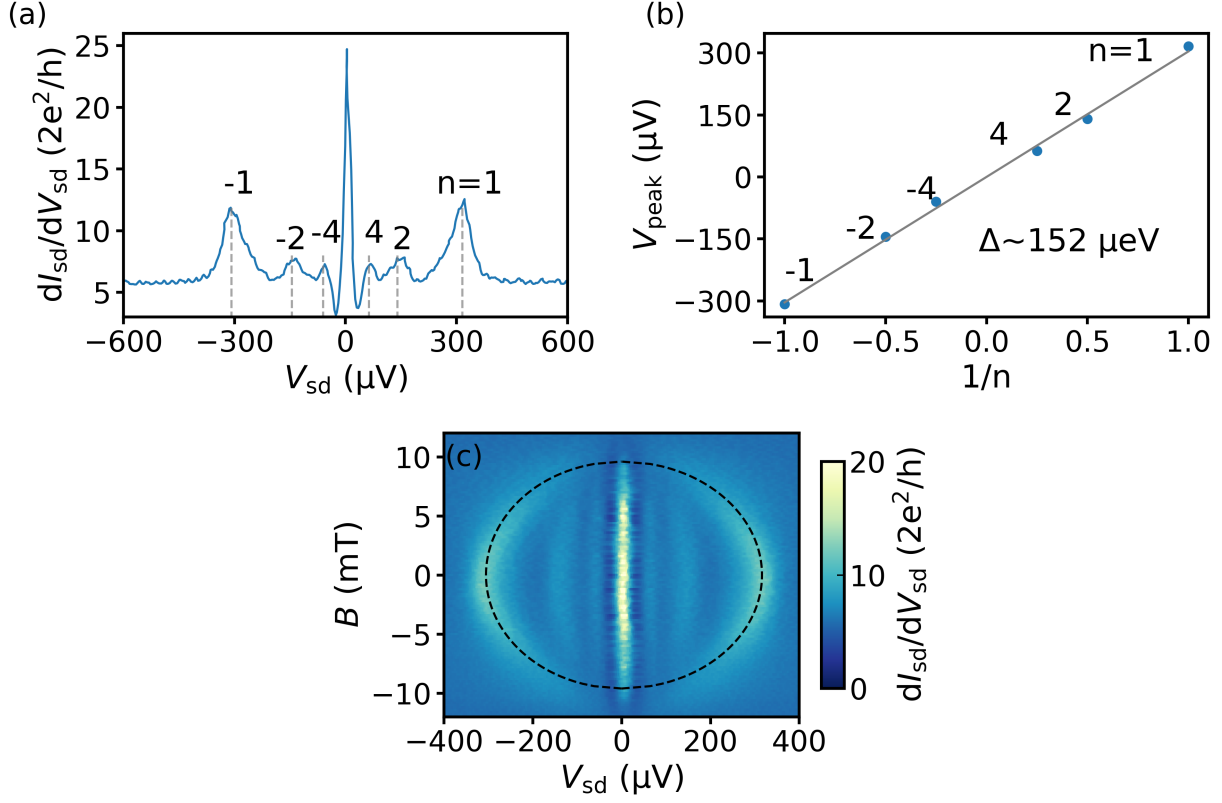


Figure S6: **Measurements of device D2 in the voltage bias configuration.** (a) Differential conductance dI_{sd}/dV_{sd} as a function of source drain voltage V_{sd} at base temperature $T \sim 20$ mK, $B = 0$ and $V_{bg} = 0$. The vertical grey dashed lines mark the positions of multiple Andreev reflection peaks and the integer numbers n denote the orders of the multiple Andreev reflection peaks. (b) Plot of the peak positions (V_{peak}) versus the inverse orders $1/n$ of the multiple Andreev reflections. The grey line is the linear fit of the data points. The superconducting energy gap determined from the slope of the fitting line is $\sim 152 \mu eV$. (c) Differential conductance dI_{sd}/dV_{sd} , on a color scale, measured as a function of V_{sd} and B . The black dashed line is the fitting curve of the magnetic field dependence of the peak position of the first order multiple Andreev reflections, $V_{sd} = \pm 2\Delta/e$, according to $\Delta(B) = \Delta(0)[1 - (B/B_c)^2]^{1/2}$. The extracted $\Delta(0)$ and B_c from the fit are $\sim 155 \mu eV$ and ~ 9.6 mT, respectively.

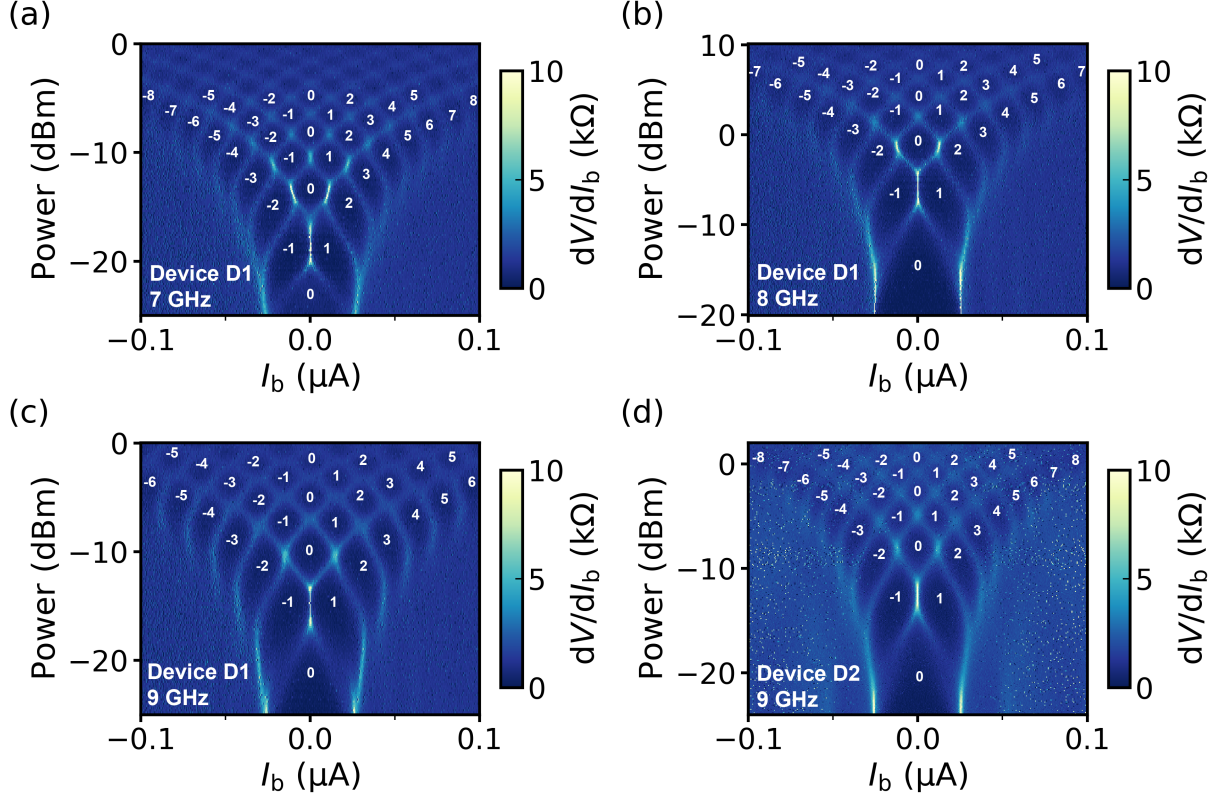


Figure S7: **Additional data of the measurements of device D1 under microwave radiation and data of the measurements of device D2 under microwave radiation.** (a), (b) and (c) Differential resistance measured for device D1 under microwave radiation as a function of bias current I_b and microwave power at microwave frequencies of $f = 7$ GHz, $f = 8$ GHz and $f = 9$ GHz, respectively, and at $V_{bg} = 0$ V, $B = 0$ and $T \sim 20$ mK. The dark blue areas marked by integer numbers n are the regions where the Shapiro steps of orders n are observed. (d) The same as in panels (a) to (c), but for the measurements of device D2 under microwave radiation at frequency $f = 9$ GHz.